Polarization Raman microprobe analysis of laser melting and etching in silicon

Cite as: Journal of Applied Physics **71**, 3492 (1992); https://doi.org/10.1063/1.350903
Submitted: 28 August 1991 • Accepted: 16 December 1991 • Published Online: 17 August 1998

Hua Tang and Irving P. Herman

Journal of Applied Physics **71**, 3492 (1992); https://doi.org/10.1063/1.350903

Polarization Raman microprobe analysis of laser melting and etching in silicon

Hua Tang and Irving P. Herman
Department of Applied Physics and the Microelectronics Sciences Laboratories, Columbia University, New York, New York 10027

(Received 28 August 1991; accepted for publication 16 December 1991)

Polarization Raman microprobe spectroscopy is used to study crystalline silicon heated to the melting point by a tightly focused cw laser beam, which is either fixed or scanned across the surface. By examining optical phonons in solid silicon, the real-time Raman spectrum monitors the progress of silicon flow during melting and the trench depth during melt-assisted etching. Raman peaks lie between 482 cm^{-1}, which is the Raman shift for silicon uniformly heated to the melting point (1690 K), and ~ 510 cm^{-1}, which is the Raman shift for *c*-Si heated just to the melting point and probed by the same beam. During laser melting with a static laser, the Raman spectrum of scattered light with $z(x,y)\bar{z}$ polarization has two peaks, while the $z(x,x)\bar{z}$ spectrum has one peak. This shows that at the beginning of melting in vacuum by a static laser there is a central region with solid silicon floating in the melt, which is surrounded by hot solid material. Because of the flow of the molten semiconductor, the temperature profile changes, causing the Raman spectrum to change rapidly. Laser melting of *c*-Ge and thin films of silicon in vacuum is also studied, as is the melting of *c*-Si by a static laser in the presence of an inert buffer gas. The presence of an inert buffer is shown to affect the temperature profile very strongly during melting and also during laser heating at lower laser powers when no melting occurs. During scanned laser melting and etching, the Raman spectrum has a single peak using either polarization configuration. Raman analysis during melting of silicon by a scanning laser shows that the average temperature in the probed region is much higher when there is a gas-phase argon buffer present (and no etching) than when there is an etching mixture of argon/chlorine gas (and etching). Along with these real-time Raman measurements, the reflection of the incident laser was monitored, and post-process Raman analysis and profilometry were also performed to characterize surface changes due to melting and etching.

I. INTRODUCTION

The melting and resolidification of semiconductors have been investigated intensively in this past decade, with much of this work focused on the laser annealing and recrystallization of thin silicon films.[1–4] The numerous studies of recrystallization of silicon thin films by scanning focused lasers, incoherent light sources, and electron beams were primarily concerned with the grain structure of the film after processing.[5] The studies of melting and resolidification of large areas in semiconductors by pulsed lasers were mostly concerned with fundamental kinetic issues such as the velocities of the melt and resolidification fronts.[6–8] Semiconductor melting has also proved to be important in several types of etching processes. For example, laser-assisted etching of silicon by gas-phase chlorine has been shown to be rapid, with etching rates up to ~ 1 cm/s, only when the silicon is locally molten.[9] According to a model of this process, this etching rate is proportional to the fraction of silicon that is molten at the reaction front.[9] Despite these many studies of semiconductor melting, little if any effort has been devoted to probing the molten region of semiconductor surfaces during melting by a tightly focused static or scanning beam. This has been due in part to the difficulty in developing real-time diagnostics to study small molten areas. In this study, polarization Raman microprobe scattering is used to examine laser melting and melt-assisted etching in silicon. Laser melting of germanium is also briefly studied. The optical methods developed here are versatile and, in particular, can be used as high-spatial resolution, real-time probes of the deposition, etching, doping, melting, and annealing of semiconductors.

It has been demonstrated that coexisting solid and liquid phases are sometimes formed when laser heating begins to melt silicon.[10–13] Complicated, stable or time-varying structures, sometimes with solid or liquid lamellae, or grating-type structures, have been observed for relatively large regions ($\sim$40–500 μm diameter) that were partially molten by static (nonscanning) cw lasers. Stable patterns were seen using $\mathrm{CO_2}$ laser heating, with solid lamellae as narrow as 3 μm wide, while time-varying patterns were observed when a laser at a shorter wavelength, such as an argon-ion laser, was used for heating.[12] The complex structure of these mixed regions has been attributed to instabilities in laser absorption and heat flow within the partially molten regions, because the molten regions reflect more (reflectivity $\sim 70\%$) than the solid regions ($\sim 40\%$). Each of these studies involved melting silicon films that were much thinner than the laser spot size.

The heat flow equation has been solved to examine melting of surfaces by static cw, pulsed, and scanning beams. Several of these calculations examined the dynamics of the melt and emphasized the temperature profile or the flow of molten material,[14–17] while others addressed the

0021-8979/92/073492-14$04.00

more microscopic features of liquid/solid phase coexistence.[18] In one of these studies, Cline and Anthony[14,15] showed how depressions can form in these molten regions because surface tension is lower in the hotter, more central molten areas than in the colder, surrounding molten regions. They showed that in laser melting of bulk materials surface tensions gradients are countered by gravity, while for local laser melting of thin films they are countered by capillary forces (surface tension).[14,15] Capillary forces are also the dominant countering forces in laser melting of bulk materials by tightly focused lasers (~ 1 μm). This leads to a ridged post-melt morphology that has been observed in several studies.[19–21] Central depressed regions have been seen in pyrolytic deposition in direct laser writing using static and scanning lasers, which have been attributed by some to melting phenomena.[22–26]

Laser-assisted etching of Si by chlorine has been studied extensively.[9,27] If the laser does not melt the surface, etching occurs by the reaction of the solid surface with Cl atoms that are produced by Cl_2 photodissociation. The etch rate is much faster when the surface is melted by the laser, where a thermally activated etching process dominates and the etching of silicon by photodissociated Cl atoms is negligible.[9,27]

Raman spectroscopy studies have shown that the frequency of zone-center optical phonons in silicon decreases monotonically from 520 cm^{-1} at room temperature to 482 cm^{-1} at the melting point (1690 K).[28] In germanium, the phonon frequency decreases from 301 cm^{-1} (300 K) to 281 cm^{-1} at melting (1210 K).[28] This temperature dependence of the Raman shift has been used to probe local wafer temperature *in situ*.[29–31] When the laser is used to probe a region with temperature variations, the temperature profile must be deduced by spatially integrating the Raman spectra over regions with different temperatures and consequently different phonon frequencies.[29–31] In some cases, temperature variations are so abrupt that this temperature averaging is significant even when a Raman microprobe is used.[31]

Nemanich *et al.*[32] used Raman scattering to examine silicon films that were partially molten within $\sim$200-μm-diam spots. A CO_2 laser was used to heat the silicon films on quartz to form these stable, coexisting solid and liquid regions at the melting temperature.[32] The Raman shift and linewidth of solid Si at the melting point were then measured. Totally, molten Si was shown to have no observable Raman spectrum.

In crystalline Si and Ge with a (001) surface, Raman scattering in backscattering configuration is allowed using the $z(x,y)\bar{z}$ polarization configuration and is forbidden in the $z(x,x)\bar{z}$ configuration, where x is the polarization of the incident laser.[33] [Standard notation is used: $z(x,y)\bar{z}=$ laser direction (laser polarization, analyzed Raman photon polarization) Raman photon direction.] The observation of a Raman signal from these samples with x polarization during or after surface processing can indicate two things: either (1) the crystal structure has locally rotated about the z axis, which can happen when solid chunks of material float in a melt or if the material becomes polycrystalline after solidifying, or (2) the surface is no longer (001), which means that after probe laser transmission and refraction at the interface the laser no longer propagates along the z axis of the material.

Recently, the authors used a tightly focused, nonscanning argon-ion laser (5145 Å) to melt c-Si and c-Ge wafers and to probe them by polarization Raman scattering.[28] In the $z(x,x)\bar{z}$ polarization configuration, a Raman peak was observed only when there was melting. This peak was attributed to solid pieces of the semiconductor floating in the melt, and was used to determine the zone-center optical phonon frequency and linewidth of solid Si and Ge at their respective melting points, which was the purpose of that study. The $z(x,y)\bar{z}$ spectrum had two peaks, one due to the solid matherial floating in the melt and the other due to hot solid material in the periphery that had never been melted. It was noticed, however, that in some cases the Raman spectrum of these partially molten surfaces changed with time and were very dependent on laser intensity. These phenomena are examined here in more detail. Melting and melt-induced etching in c-Si are studied using both static and scanning lasers. Melting of Si films and c-Ge by a static laser is also examined briefly.

Experimental methods are detailed in Sec. II. In Sec. III, experimental observations are presented separately for laser heating and melting by a static laser in vacuum, laser heating and melting by a static laser in the presence of a buffer gas, laser melting by a scanning laser in a vacuum or buffer gas, and laser etching by a scanning laser. Section IV separately discusses the implications of these results and conclusions are presented in Sec. V.

II. EXPERIMENTAL PROCEDURE

Laser-heated c-Si (001) and c-Ge (001) wafers were examined in $z(x,y)\bar{z}$ and $z(x,x)\bar{z}$ orientations, where x,y are the crystal [100] and [010] directions and x is also the laser polarization direction. Epitaxial silicon films on sapphire and polycrystalline silicon films on sapphire and quartz were also examined. Each of these films was 0.6 μm thick.

A linearly polarized cw argon-ion laser (5145 Å) was focused on the semiconductor surface to a spot size ranging from 0.8 to 1.0 μm (half width of intensity decrease to $1/e$), depending on the focusing optics used. The sample was placed in a vacuum chamber, which was mounted on a motorized x-y translation stage to permit scanning the laser across the surface at speeds up to 200 μm/s. Unless otherwise specified, the sample was scanned in the x direction, i.e., parallel to the polarization of the laser. Laser melting experiments were conducted in vacuum ($\sim 10^{-4}$ Torr) or in the presence of argon, and laser etching experiments were conducted in argon/chlorine mixtures. To compare etching and melting, the etching experiments were conducted using the same partial pressures of argon used for melting, but with a small additional partial pressure of the chlorine gas etchant.

The focused laser beam heated the sample and also provided photons for the spontaneous Raman spectrum.

Only the central ~2 μm of the partially molten region was examined by this probe. The backscattered Stokes Raman signal was transmitted through a rotatable λ/2 wave plate, followed by a beam splitter that transmitted light that was linearly polarized in a fixed direction. This polarization-analyzed Raman signal was measured by the detection system, consisting of a triple spectrometer and an intensified diode array. The detection efficiency of $z(x,x)\bar{z}$ scattered light was 0.4× that of $z(x,y)\bar{z}$ light. The polarization discrimination was such that only 1% of y-polarized scattered photons $[z(x,y)\bar{z}]$ leaked into the $z(x,x)\bar{z}$ channel.

In experiments using a static laser to melt the surface, time-resolved Raman spectra were taken with up to ~0.1 s resolution. In experiments where the laser was scanned across the surface, Raman analysis probes the moving melt front in steady state. The dwell time of the laser at any point within the scan in these scanning experiments is the spot size/scan speed, which was ~8 ms for the fastest scan rates.

As detailed in Sec. III, the conditions for the etching experiments were sometimes chosen so that the depth of the etch trench was small compared to the maximum etch depth obtainable in the scanned etching experiments. This experimentally observed maximum etch depth depends on laser focusing conditions and gas transport, and was typically ~0.6 μm in experiments with 0.7 Torr Cl_2 plus 100 Torr Ar. With this criterion met, the laser probes the reaction front while it is still being etched. Otherwise, the laser probes an already etched trench. Also, under these conditions relatively shallow trenches are etched and consequently all surfaces remain nearly normal to the laser during and after etching. (This is important for polarization analysis, as was mentioned in the Introduction.) Such relatively slow etching conditions suggested the use of reaction mixtures with relatively low chlorine and relatively high argon buffer partial pressures.

Surface melting was determined in several ways. In some cases the occurrence of melting is clear from features in the Raman spectrum, as will be seen later. When the flow of the molten semiconductor leads to surface roughness $\gg\lambda/10$ while the laser is still incident, the reflected beam will diverge into a very wide angle, which also indicates melting. A swirling reflection pattern is seen if this surface morphology changes in time. Because such wide-angle and swirling reflection patterns are observed in these microheating experiments, measuring changes in the magnitude of the reflected intensity upon melting is not a reliable probe. Post processing Raman analysis and *ex situ* profilometry were also used to determine the movement of molten material.

III. EXPERIMENTAL RESULTS

A. Laser melting with a static laser—in vacuum

For low laser powers, Raman signals are observed with $z(x,y)\bar{z}$ polarization for the crystalline samples (c-Si, c-Ge, and epi Si film), while no $z(x,x)\bar{z}$ signals are observed. The same Raman spectrum is observed for both analyzed polarizations for laser-heated polycrystalline silicon films. In all cases studied, the Raman shift decreases monotonically with increasing laser power (P) up to the power where melting begins (P_m). The onset of melting was indicated both by changes in the Raman spectrum and by the characteristic large-angle, swirling nature of the reflection pattern. These experiments were conducted in vacuum with a static laser.

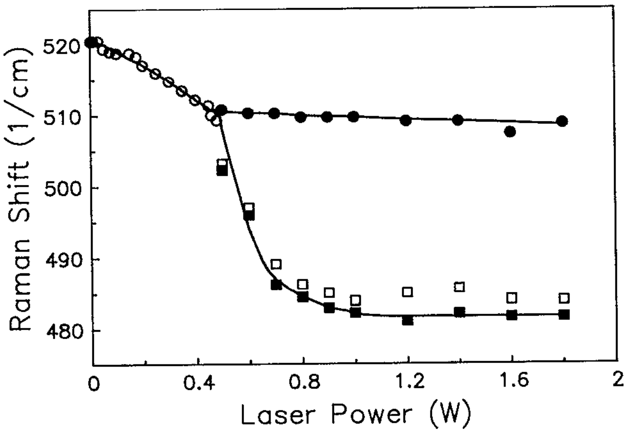

FIG. 1. Raman shift during static laser heating of c-Si as a function of laser power for two analysis polarizations, accumulated during the first 0.5 s of laser heating (5145 Å). For $P<P_m=0.5$ W, Raman signals can be seen only in the $z(x,y)\bar{z}$ configuration (open circles). For $P>P_m$, two peaks are seen in $z(x,y)\bar{z}$ configuration (solid circles and open squares, fit as the sum of two Lorentzians) and one peak is seen for $z(x,x)\bar{z}$ (solid squares).

The Stokes shift in c-Si decreases from 520 cm^{-1} at room temperature to ~510 cm^{-1} for $P_m=0.5$ W (0.9 μm spot size), as seen in Fig. 1. For Si films on sapphire and quartz, the lineshifts decrease from 522 and 519 cm^{-1} (300 K) to ~507 and ~499 cm^{-1} for $P_m=0.25$ and 0.025 W, respectively. This is shown for the epi Si film on sapphire in Fig. 2. In c-Ge, the Raman shift decreases from 300 cm^{-1} at room temperature to ~292 cm^{-1} for $P_m=0.14$ W (Fig. 3). As the laser power approaches P_m,

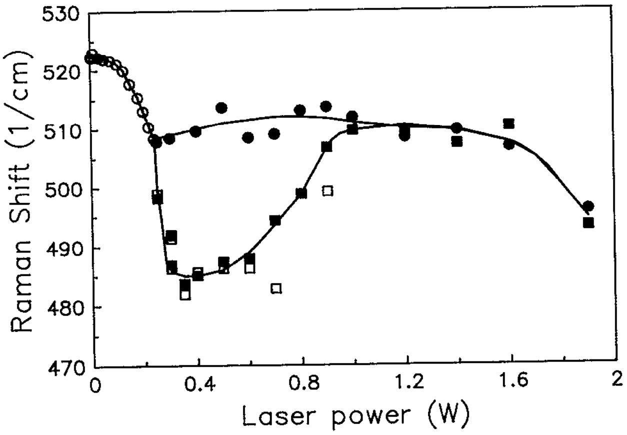

FIG. 2. Raman shift during static laser heating of an epi Si film (0.6 μm thick) on sapphire as a function of laser power for two analysis polarizations, as in Fig. 1 ($P_m=0.25$ W). Note that the low-energy peak is merged into the high-energy peak for $P>1.0$ W.

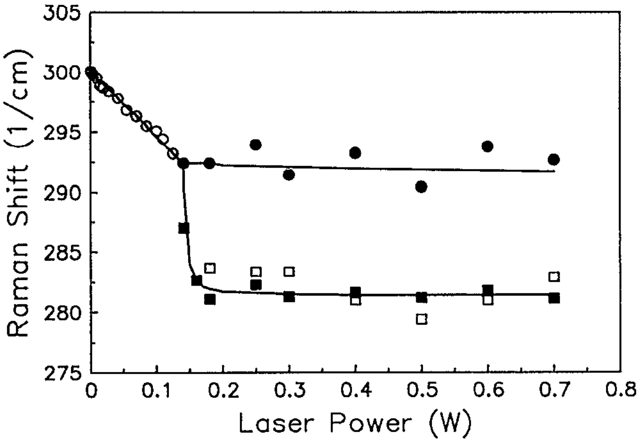

FIG. 3. Raman shift during static laser heating of *c*-Ge as a function of laser power for two analysis polarizations, as in Fig. 1 ($P_m = 0.14$ W).

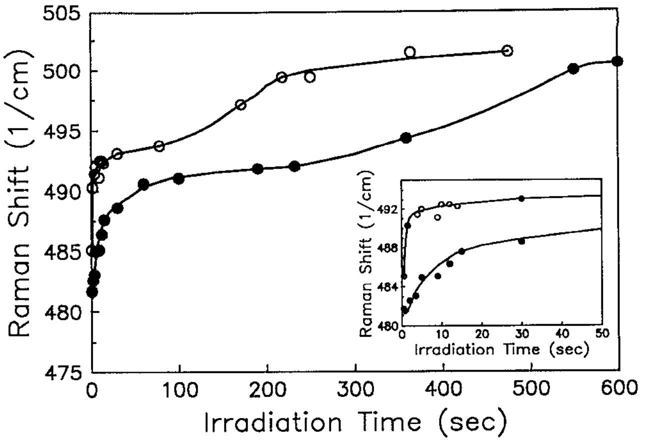

FIG. 5. Shift of the $z(x,x)\bar{z}$ Raman peak of partially molten *c*-Si as a function of irradiation time (t) during static laser-induced melting in vacuum. The open and solid circles correspond to $P = 0.8$ and 1.5 W, respectively. The kinks at ~10 and 50 s for 0.8 and 1.5 W, respectively, correspond to t_1 and those at ~250 and 550 s correspond to t_2.

the *c*-Si spectra become asymmetric due to a long tail on the low-frequency side, while the *c*-Ge spectra remain symmetric.

The Raman spectra are very different when the semiconductor is partially molten ($P > P_m$). For $z(x,x)\bar{z}$, a single peak appears in the *c*-Si, epi Si film, and *c*-Ge Raman spectra (Fig. 4). For $z(x,y)\bar{z}$, the Raman spectrum is more complex; at times two peaks are seen (Fig. 4), while at other times only one peak is seen.

For partially molten *c*-Si, the peak in the $z(x,x)\bar{z}$ Raman spectrum is at 501 ± 1 cm^{-1} for 0.5 W and decreases to the constant value 481.7 ± 0.4 cm^{-1} for 1.0–1.8 W (Fig. 1).[28] These spectra were accumulated from $t = 0$–0.5 s, where $t = 0$ denotes the onset of cw laser heating. For $t > 0.5$ s, the Raman shift quickly increases until t_1, which ranges from ~10–50 s, then slowly increases to and remains at 501.6 cm^{-1} (Fig. 5). The time needed to reach this final steady state (t_2) is on the order of several minutes. Both t_1 and t_2 increase monotonically with P, as is demonstrated in Fig. 5. For $P = 0.5$ W (~P_m) to ~0.6 W, this $z(x,x)\bar{z}$ peak sometimes jumps back and forth between ~490 and 501 cm^{-1} in the first ~10 s of melting before settling at 501 cm^{-1}. In general, the observed reflection pattern swirls until $t = t_1$. Afterwards, the reflection pattern does not swirl but fluctuates somewhat.

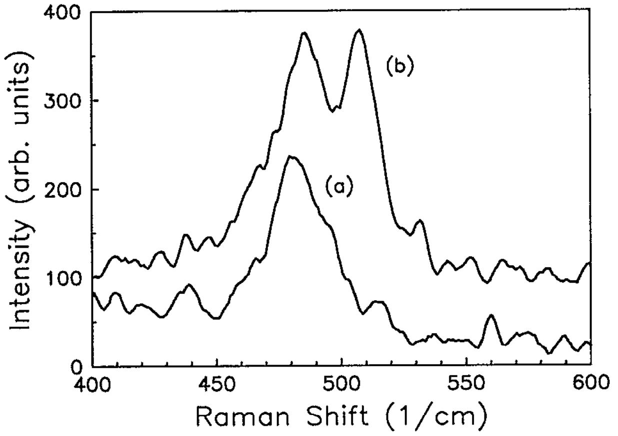

FIG. 4. Raman spectra of laser melted *c*-Si averaged for the first 0.5 s of sample heating by a static laser with $P = 1.2$ W ($> P_m$) at 5145 Å. (a) For $z(x,x)\bar{z}$ analysis only one peak is seen, at 481.3 cm^{-1}, while (b) for $z(x,y)\bar{z}$ Raman analysis two peaks are observed, at 508.4 and 484.4 cm^{-1}.

For $z(x,x)\bar{z}$, a single Raman peak is also seen in *c*-Ge sample for $P > P_m$. The shift of this peak decreases from ~287 cm^{-1} to 281.4 ± 0.5 cm^{-1} as the laser power increases from 0.14 to 0.18 W, and stays at the latter value for higher powers.[28] For $P > 0.18$ W, this Raman shift is constant during at least the first 10 s of melting, and then it moves towards 288 cm^{-1}, though more slowly than in the laser melting of *c*-Si. For example, for $P = 0.4$ W, there is no change in the shift for the first 100 s, and then the peak slowly moves back to 288 cm^{-1} during the next 8–10 min. For 0.6 W, the peak stays at 281.8 cm^{-1} for more than 5 min.

The linewidths (FWHM) in these $z(x,x)\bar{z}$ spectra of partially molten material are 24.3 ± 0.3 cm^{-1} and 14.1 ± 0.5 cm^{-1} for *c*-Si ($P = 0.9$–1.9 W) and *c*-Ge ($P > P_m$), respectively ($t = 0$–0.5 s, corrected for instrumental resolution).[28] As with the Raman shift, the Raman line shape for *c*-Si is different in the lower-power melting range (0.4–0.8 W) than in the higher power range (0.9–1.9 W). For these lower laser powers, the Raman peaks are broader by ~4 cm^{-1} and are more asymmetric than for higher powers.

The $z(x,y)\bar{z}$ spectrum of partially molten *c*-Si evolves in a complex manner when $P > P_m$. Typically two peaks appear at the beginning of irradiation (Fig. 4). The data in Figs. 1–3 were obtained by fitting these early spectra ($t = 0$–0.5 s) as the sum of two Lorentzians. For *c*-Si, the high-energy peak is located at ~510 cm^{-1}, which is reminiscent of that seen for $P \lesssim P_m$. The other peak is at slightly higher energy than the $z(x,x)\bar{z}$ single peak (by ~3 cm^{-1}). When an asymmetric line shape is used to model the high-energy peak (similar to that used to fit the $P < P_m$ data, as is justified later), the low-frequency $z(x,y)\bar{z}$ peak

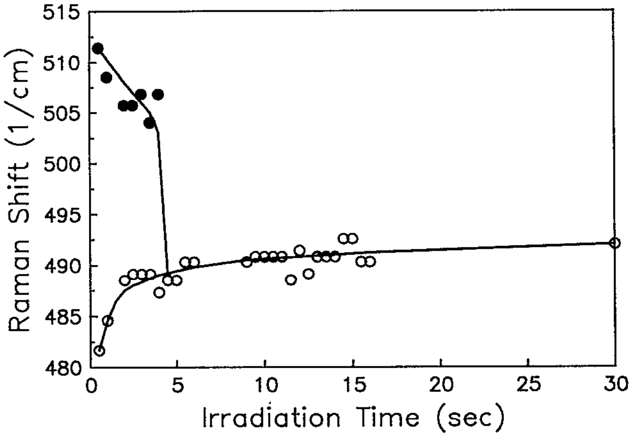

FIG. 6. Shift of the $z(x,y)\bar{z}$ Raman peak(s) as a function of irradiation time for *c*-Si melted by a static laser in vacuum (1.0 W). Initially, there are peaks at ~482 and ~511 cm^{-1}. The high-energy peak (solid circles) later merges into the low-energy one (open circles) and becomes a single peak at $t = \sim 5$ s. This peak is asymmetric, with a longer tail at high frequency, and becomes more symmetric later. After ~30 s, there are no obvious differences between the $z(x,x)\bar{z}$ and $z(x,y)\bar{z}$ Raman spectra.

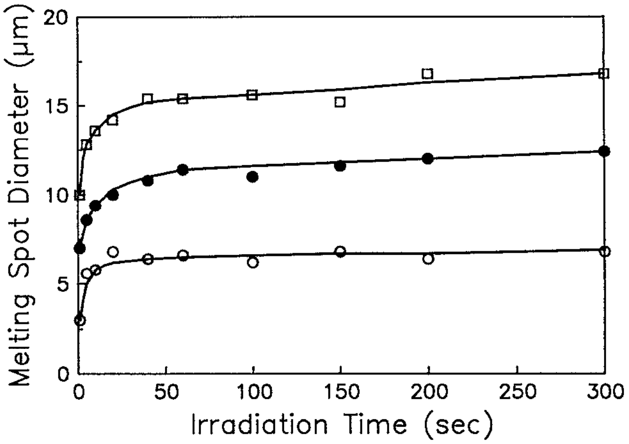

FIG. 7. Post-melting diameter of laser molten spots as a function of irradiation of time (t) for static laser melting of *c*-Si using different laser powers. These diameters were determined by profilometry and represent the outer extent of molten flow. Each profilometry trace had a raised outer ring (whose outside diameter is plotted here) and a central dip. The open circles, solid circles and open squares corresponding $P = 0.46$, 0.80, and 1.20 W, respectively.

and the $z(x,x)\bar{z}$ peak coincide. After calibration, the low-energy $z(x,y)\bar{z}$ peak and the $z(x,x)\bar{z}$ peak have the same height.

After the onset of laser melting in *c*-Si, the two peaks in the $z(x,y)\bar{z}$ spectrum move toward each other and merge into one peak, as seen in Fig. 6. This pattern is most clearly seen for $P > 0.8$ W. As they begin to merge ($t = 0$–5 s), the low-energy peak gets stronger (by a factor of 1.5), while the high-energy peak gets weaker (by a factor of 0.7) and eventually disappears within the other peak. This combined $z(x,y)\bar{z}$ peak becomes narrower and more symmetric as it moves to 501 cm^{-1}. After $t \sim 30$ s, and during this several-minute-long movement to 501 cm^{-1}, the $z(x,y)\bar{z}$ and $z(x,x)\bar{z}$ spectra are identical.

In one experiment, *c*-Si was melted with 1.6 W and the Raman spectrum evolved to steady state at $t = t_2$. Then the Raman spectrum and the reflection pattern were monitored as the laser power was slowly decreased. The $z(x,y)\bar{z}$ and $z(x,x)\bar{z}$ Raman shifts increased monotonically and the reflection pattern continued to have small fluctuations as the laser power was decreased to 0.66 W. At this power, the Raman shift was ~511 cm^{-1} and the reflection pattern stopped fluctuating. Below this power, the Raman shift continued to decrease, as in Fig. 1, and the reflection pattern did not change anymore.

In partially molten *c*-Ge, the high-energy $z(x,y)\bar{z}$ peak is ~293 cm^{-1}. The low-energy peak decreases quickly from 287 to ~281 cm^{-1} as power increases (Fig. 3, Lorentzian fit), and tracks the $z(x,x)\bar{z}$ peak. For the first ~1–2 s, the two $z(x,y)\bar{z}$ peaks have the same intensity. Later the high-energy peak becomes weaker and the low-energy peak becomes stronger. By $t = 3$ s, the high-energy peak is totally merged into the other peak. Afterwards, the Raman spectra for the two polarizations are identical.

The intensity of the $z(x,x)\bar{z}$ Raman signal decreases slowly in *c*-Si with increasing laser power ($P > P_m$, $t = 0$–0.5 s). In *c*-Ge, this intensity decreases very quickly with P, and no Raman signal is seen for $P > 0.7$ W from $t = 0$–5 s.

The laser-melted regions in *c*-Si were reexamined after melting by using profilometry and Raman spectroscopy with a low-power laser (~0.005 W). Profilometry measurements were made on regions that had been melted by the laser (0.8 μm spot size) for a given time t. They show a dip in the center and a raised outer ring,[24–27] which suggests flow of molten silicon from the laser focus outwards and possibly evaporation. Figure 7 plots the diameter of these spots as a function of irradiation time (t) for different laser powers. A rapid increase in spot size is seen in the first ~10–50 s, which is followed by a slower increase. The end of the phase of quickly increasing real-time Raman shift, the end of the swirling reflectivity pattern, and the end of rapid molten flow (as determined by profilometry) all occur at approximately the same time (t_1). Slower changes in the Raman spectrum, the reflection pattern, and molten flow then continue until t_2.

The post-melting $z(x,x)\bar{z}$ and $z(x,y)\bar{z}$ Raman spectrum intensities, lineshifts, and linewidths are the same within a circle centered about the initial laser focus (*c*-Si) after correcting for detection sensitivity (Fig. 8). The diameter of this circle is equal to that determined by profilometry within ~0.5 μm. Outside this region, peaks are seen only for $z(x,y)\bar{z}$.

For partially molten epi Si films on sapphire, there are initially two peaks in the $z(x,y)\bar{z}$ spectrum and one peak in the $z(x,x)\bar{z}$ spectrum (Fig. 2, $P > P_m$, 0–0.5 s), which is similar to that seen for laser-molten *c*-Si. When $P_m < P < 0.7$ W, two peaks are observed for both x and y analysis polarizations for the poly Si film on sapphire. For both films, the high-energy peak is near 510 cm^{-1} and the shift of the low-energy peak decreases quickly with increasing laser power from 492 cm^{-1} (0.25 W) to 484 cm^{-1} (>0.3 W). The low-energy peak begins to merge into the high-energy one for $P > 0.7$ W (0–0.5 s). At higher powers, a Raman signal from the sapphire substrate at 412 cm^{-1}

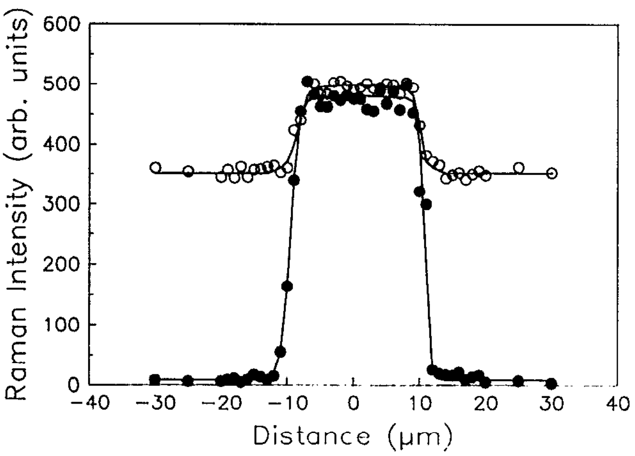

FIG. 8. Peak intensity of the Raman spectrum obtained by scanning a probe beam (~0.005 W) across a spot on *c*-Si that had been melted by a focused laser for 200 s (5145 Å, 1.4 W). For each point in the scan the Raman shift and width were within 0.5 cm^{-1} of the respective values for *c*-Si at room temperature. The solid and open circles correspond to the $z(x,x)\bar{z}$ and $z(x,y)\bar{z}$ Raman spectra, respectively. These data have been corrected for the polarization-dependent collection efficiency.

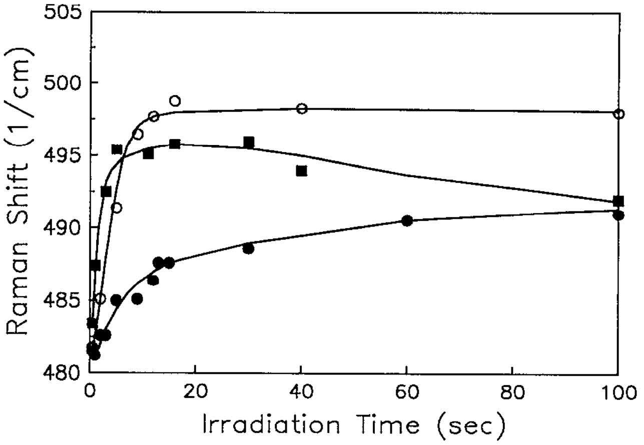

FIG. 9. Raman shift of partially molten *c*-Si heated by a static laser with $P = 1.5$ W in vacuum or in the presence of an argon buffer as a function of irradiation time for $z(x,x)\bar{z}$ polarization. The open circles and solid squares are the shifts in 10 and 700 Torr argon, respectively, and the solid circles are the shifts in vacuum.

appears, whose intensity increases rapidly with increasing power when $P > 0.7$ W.

Only one Raman peak can be identified when the poly Si film on quartz is melted (~486 cm^{-1}). The peak frequency increases to ~512 cm^{-1} when $P > 0.3$ W.

B. Laser melting with a static laser—in a gas

Static laser heating and melting of *c*-Si were also examined in the presence of an argon buffer. First, the threshold laser power needed to melt *c*-Si was measured as a function of pressure, using the change in reflectivity pattern as the melting criterion. In vacuum, $P_m = 0.54$ W (1.0 μm spot size). With added argon, P_m initially increases linearly with increasing argon partial pressure and then levels off to $P_m = 0.62$ W above ~700 Torr. Similar pressure dependences are seen for pure helium and air, with P_m increasing to 0.615 and 0.605 W, respectively, at high pressures of these two gases. The threshold melting laser power for *c*-Ge is 0.18 W (1.0 μm spot size) in vacuum, and 0.20 W in 700 Torr argon buffer.

The $z(x,x)\bar{z}$ Raman spectrum taken during the first 0.5 s of melting in *c*-Si is mildly affected by the buffer, with the peak frequency increasing from 481.7 to 483.5 cm^{-1} as the argon pressure is increased from 0 to 700 Torr ($P = 1.5$ W). The argon buffer gas has a much larger effect later during irradiation, as is shown in Fig. 9 (1.5 W). In contrast to the slow change in vacuum (10^{-4} Torr) after t_1, in the presence of argon the Raman shift increases quickly from ~483.5 to ~496 cm^{-1} in the first ~10 s, and then at lower pressures ($\lesssim 50$ Torr) it is constant and at higher pressures (> 50 Torr) it slowly decreases with time. The reflection pattern stops swirling at ~10 s when the shifts have moved to ~496 cm^{-1}.

The Raman peak during the first 0.5 s of melting *c*-Ge in vacuum is at 281.4 cm^{-1} [$z(x,x)\bar{z}$], and does not move for at least 10 min (0.6 W, 1 μm spot size), during which time the reflection pattern is swirling. With argon, the energy shift obtained in the first 0.5 s becomes slightly higher (283.6 cm^{-1} for 700 Torr argon, 0.6 W). This shift increases to ~ 290 cm^{-1} in several seconds (and no longer changes) and then the reflection pattern stops swirling (5–700 Torr).

For $z(x,y)\bar{z}$, two Raman peaks are seen during the first ~1–2 s of melting *c*-Si and *c*-Ge in the presence of a buffer gas, as is the case in vacuum. The high-energy peak later merges into the low-energy one, and after ~20 s the *x*- and *y*-polarized Raman spectra are identical.

Spots melted with argon present were reexamined by profilometry. After melting in vacuum for < 100 s, a typical recrystallized spot has a small dip at the center and a raised outer ring. The profile of these molten spots in *c*-Si are similar in vacuum and in argon gas. However, when the silicon was melted by a high laser power (1.6 W) in vacuum for more than ~200 s, the hole seen at the center is much deeper than those made under similar conditions, but in the presence of argon. The profiles of laser melting of *c*-Ge in vacuum and argon are similar to those for short irradiation times in *c*-Si, except that the central dips formed by melting in the presence of argon are usually slightly deeper than those melted in vacuum. Profiles of Si melted in the presence of chlorine showed a central hole but no raised outer ring.

C. Laser melting with a scanning laser

Raman spectra were averaged over 10 s during each run of scanned laser melting and etching of *c*-Si. A fixed laser power of 1.6 W was used, which far exceeds that needed to achieve melting in vacuum (0.5 W for the 0.9 μm spot size) or with gas present. The Raman spectra under scanning conditions always consist of a single peak, which is sometimes asymmetric. Representative spectra are shown in Fig. 10. The Raman shifts and linewidths during scanned melting in vacuum are shown in Figs. 11(a) and 12(a), respectively, for both $z(x,x)\bar{z}$ and $z(x,y)\bar{z}$ analysis

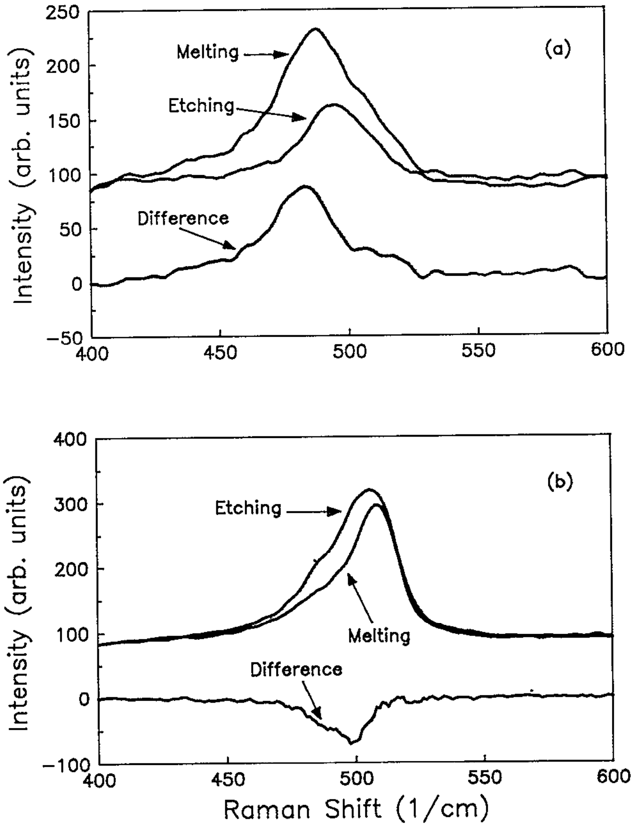

FIG. 10. Raman spectra during melting (100 Torr argon) and melting-induced etching (0.7 Torr chlorine/100 Torr argon, mixture B), and the difference between these two spectra for a $P = 1.6$ W laser scanning in the x direction at 40 μm/s on c-Si (regime II). (a) For $z(x,x)\bar{z}$ polarization, the peaks of the melting (only), the melting-induced etching, and the difference spectra are at 487, 494, and 482 cm^{-1}, respectively. (b) For $z(x,y)\bar{z}$ polarization, the peaks of the melting (only), the melting-induced etching, and the difference spectra are at 508, 504, and 496 cm^{-1}, respectively. These data have been corrected for the polarization-dependent collection efficiency, and the ordinate scales in (a) and (b) are the same. Note that the intensity of the $z(x,y)\bar{z}$ Raman peak increases by a factor of ~ 1.5, while that of the $z(x,x)\bar{z}$ peak decreases by a factor of ~ 2, as the scan speed increases from 20 to 200 μm/s during melting (only).

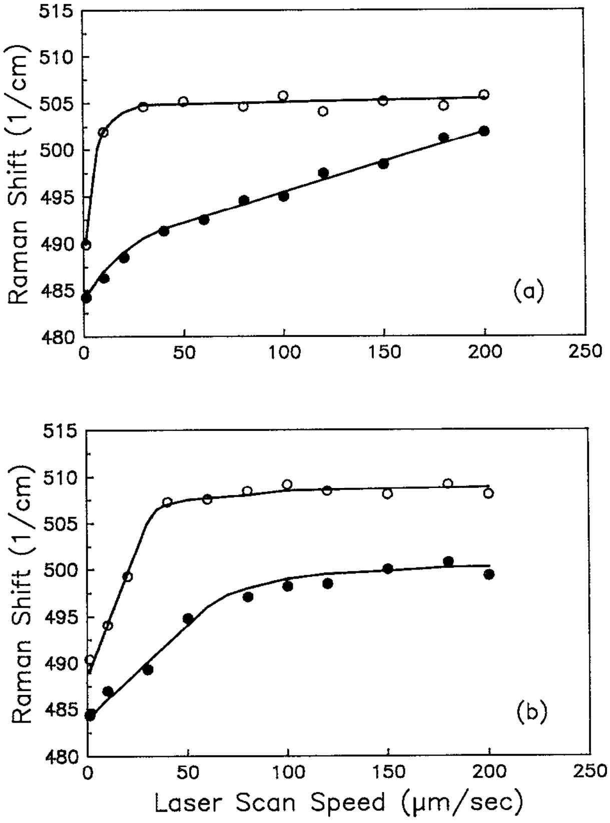

FIG. 11. Raman shift as a function of laser scan speed during c-Si melting by a scanning laser (1.6 W) for $z(x,x)\bar{z}$ (solid circles) and $z(x,y)\bar{z}$ (open circles) polarization (a) in vacuum and (b) in the presence of 100 Torr argon.

as functions of laser scan speed. Similar data taken in the presence of 100 Torr argon are plotted in Figs. 11(b) and 12(b). With some exceptions, these figures show an increase in shift and decrease in linewidth with increasing scan speed. Though addition of argon does change the Raman profile somewhat, the overall trends are the same as in vacuum. The $z(x,y)\bar{z}$ Raman scattering intensity during melting both in vacuum and with an argon buffer is approximately twice as large as the $z(x,x)\bar{z}$ intensity when the scan speed is 20 μm/s. The intensity of the y-polarized Raman peak increases by a factor of 1.5, while that of the x-polarized peak decreases by a factor of 2, as the scan speed increases from 20 to 200 μm/s in vacuum or with an argon buffer present.

The minimum laser power needed to melt c-Si during a scan, as determined by the changed reflection pattern upon melting, increases with increasing argon pressure (as was observed for laser melting with a static laser) and with increasing scan speed. For example, in vacuum P_m is 0.54 W for a static laser (1.0 μm spot size) and increases to 0.60 W as the scan speed increases to 200 μm/s. Similarly, in the presence of 700 Torr argon this threshold power increases from 0.62 to 0.68 W as the scan speed increases from 0 to 200 μm/s. For laser powers slightly lower than the melting threshold, the $z(x,y)\bar{z}$ Raman shift is ~ 510 cm^{-1} and the linewidth is ~ 16.5 cm^{-1} for all scan speeds, including during static laser heating, and for laser heating in vacuum or argon.

At corresponding laser powers and scan rates, profilometry traces across laser melting scans in c-Si look roughly the same for vacuum and 100 Torr argon experiments. As an example, when the laser scan rate is 100 μm/s ($P = 1.6$ W) a 2-μm-wide and 0.1-μm-deep trench is formed in both cases, which has 0.2-μm-high ridges extending above the surface on either side that are separated by 4 μm. (The trench depth measurement may be smaller than the actual depth because of the finite profilometer tip width.) These trench dimensions tend to increase very sublinearly with increasing dwell time (decreasing scan rate).

D. Laser etching of Si with a scanning laser

Before conducting the Raman probing experiments in real time during etching, laser etching of c-Si was examined using *ex situ* profilometry to assess the relative importance of etching and melting. The "etch" depth during melting in the presence of 100 Torr Ar is $\sim$ 0.2 μm at very slow

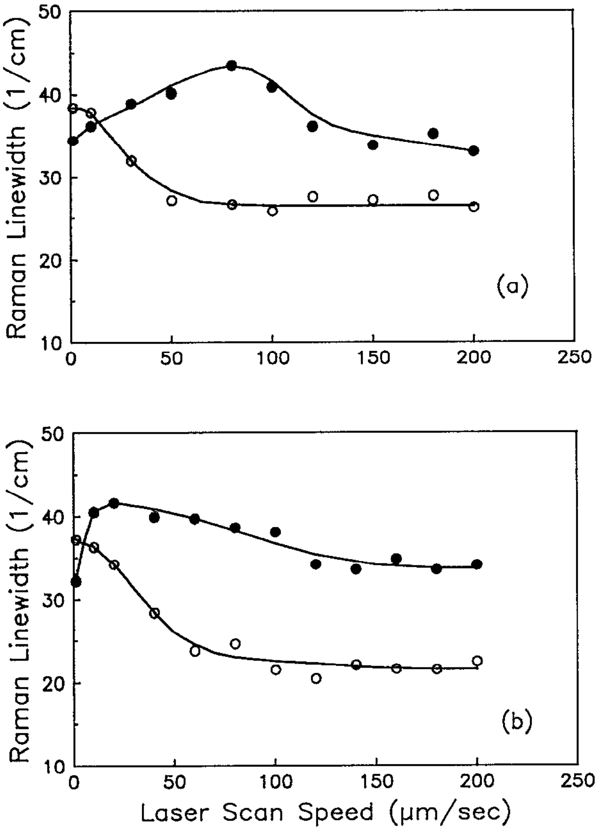

FIG. 12. Raman linewidth (full width at half maximum) as a function of laser scan speed during *c*-Si melting by a scanning laser (1.6 W) for $z(x,x)\bar{z}$ (solid circles) and $z(x,y)\bar{z}$ (open circles) polarization (a) in vacuum and (b) in the presence of 100 Torr argon.

speeds, decreases to ~0.1 μm for ~40 μm/s scan speed, and essentially remains at that value for faster speeds. The dependence of the etch depth on the scan rate for different etch mixtures (0.3 Torr Cl_2/100 Torr Ar, mixture A; 0.7 Torr Cl_2/100 Torr Ar, mixture B) is shown in Fig. 13. These etch depths are in agreement with the work of Treyz *et al.*[9] Three experimental regimes can be identified by using this figure.

(I) Little etching occurs relative to melt-induced flow. This regime occurs when the laser scans fast on *c*-Si in the presence of a high argon pressure and low chlorine pressure. The transverse profilometry scans are the same for scanning laser melting in the presence of either 100 Torr pure Ar, mixture A when the laser scan speed is >140 μm/s, or mixture B for speeds >180 μm/s ($P=1.6$ W).

(II) Etching is fast relative to melt-induced flow, but slow enough so that the "maximum" etch depth is not reached. This regime occurs for laser scan speeds between 20 and 140 μm/s for mixture A, and for speeds between 40 and 180 μm/s for mixture B. Profilometry shows that in this regime the etched line depth is inversely proportional to the laser scan speed. In the fast scan limit (approaching regime I), the depth of the melted line is ~0.1 μm for each condition, and is mainly due to the melt-induced flow. In the low scan speed limit (approaching regime III), the depth is ~0.4 μm for mixture A and ~0.6 μm for mixture B. Only in regime II is the entire probed region undergoing etching.

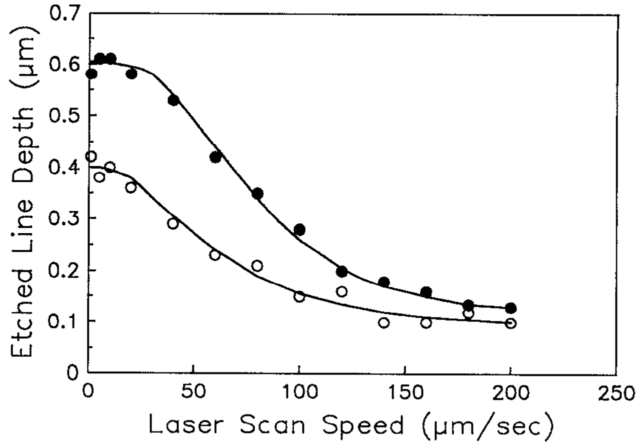

FIG. 13. Profilometry measurement of the etched line depth vs laser scan speed after *c*-Si melting-induced etching (1.6 W). The etchants are 0.3 Torr Cl_2/100 Torr Ar (mixture A, open circles) and 0.7 Torr Cl_2/100 Torr Ar (mixture B, solid circles).

(III) Etching is so fast that the etch depth reaches its maximum value before the main part of the scanning laser has reached that spot. The etched line depth does not change with the laser scan speed for laser scans slower than 15 μm/s for mixture A and 30 μm/s for mixture B.

Raman spectra were taken with both *x*- and *y*-polarization analysis during melting, with the laser scanning in the *x* direction across the *c*-Si surface in the presence of either 100 Torr pure Ar or an etching mixture. Typical Raman spectra during melt (only) and melt-induced etching are shown in Figs. 10(a) and 10(b) for $z(x,x)\bar{z}$ and $z(x,y)\bar{z}$ analysis, respectively (40 μm/s scan speed, mixture B, regime II). In both parts of the figure, the lowest of the three curves represents the difference of these two Raman spectra, which is obtained by subtracting the spectrum taken during melt-induced etching from the corresponding spectrum during melting. For $z(x,x)\bar{z}$ the peaks during the melting (only) are up to ~100% larger than during etching, while for $z(x,y)\bar{z}$ the intensities are much more nearly equal, with the spectra during melting typically being up to ~20% smaller than the Raman peak during etching.

For $z(x,x)\bar{z}$, the Raman peaks obtained during a 40-μm/s scan are at ~487 and ~494 cm^{-1} for pure argon and the etching mixture, respectively. These shifts increase to ~500 and 507 cm^{-1}, respectively, with increasing scan speed (up to 200 μm/s). For most scan speeds these peaks are much broader than those obtained during static laser beam melting, and are asymmetric, with longer tails at low energy. For speeds <5 μm/s, the Raman spectra are only slightly broader than static melting Raman peaks and are symmetric. For speeds $>\sim 40$ μm/s (regimes II and III), the Raman spectra obtained in the presence of pure argon are stronger and more skewed to lower energy than those obtained with the etching mixture.

The difference spectra for $z(x,x)\bar{z}$ are shown in Fig. 14 for different laser scan speeds (>40 μm/s, mixture B).

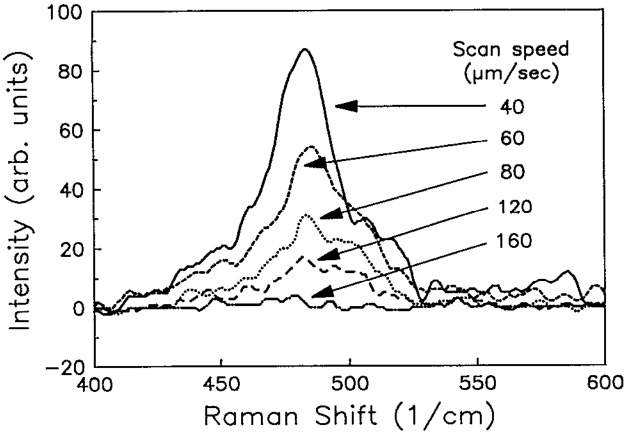

FIG. 14. Difference between $z(x,x)\bar{z}$ Raman spectra taken during *c*-Si melting (100 Torr argon) and melting-induced etching (0.7 Torr Cl_2/100 Torr Ar, mixture B) for a 1.6 W (5145 Å) laser scan in the *x* direction at different scan speeds. For slow scan speeds, ~30–40 μm/s, this difference peak is at ~482 cm^{-1} and has a linewidth of ~25 cm^{-1}. With increasing laser scan speed the peak becomes smaller, moves towards ~490 cm^{-1}, and becomes broader.

The peak magnitude of these difference spectra is plotted as a function of laser scan speed in Fig. 15 for mixtures A and B. As with the profilometry measurements, three regimes can be identified. For fast scans ($\gtrsim$ 140 μm/s for mixture A and $\gtrsim$ 180 μm/s for mixture B, as in regime I), the melt and melt-induced spectra are very similar and therefore the differences are close to zero. The magnitude of the difference spectrum increases monotonically with decreasing scan speed (regime II). These differences are nearly independent of laser scan speed for speeds $\lesssim$ 20 and ~20–40 μm/s with mixtures A and B, respectively (regime III). When the laser scan speed is extremely slow (~1–10 μm/s, regime III), the height of the difference spectrum decreases and becomes negative for mixture B.

The $z(x,y)\bar{z}$ Raman spectrum changes with scan speed during etching (mixture B) in the same way as for pure melting. The line shape is asymmetric (except for < 5 μm/s) with a longer tail at low energy. The height of the $z(x,y)\bar{z}$ difference spectrum, which is defined as before, is negative, meaning that the magnitude of the Raman spectrum taken during etching is larger than that during melting. This is in contrast to that for $z(x,x)\bar{z}$ polarization.

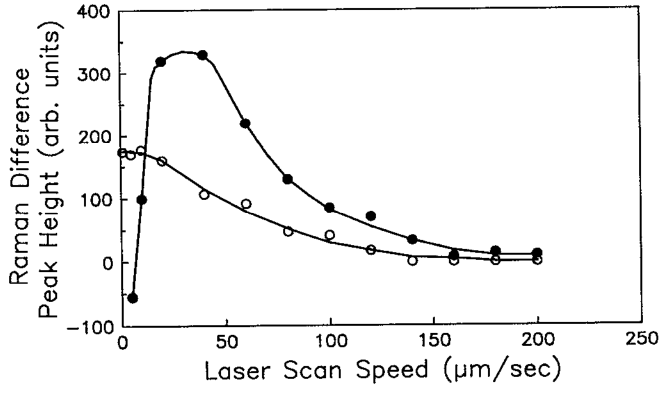

FIG. 15. Peak height of the difference between the $z(x,x)\bar{z}$ Raman spectra during *c*-Si melting (100 Torr argon) and melting-assisted etching using either mixture A (open circles) or mixture B (solid circles) during scanning by a laser (1.6 W) in the *x* direction.

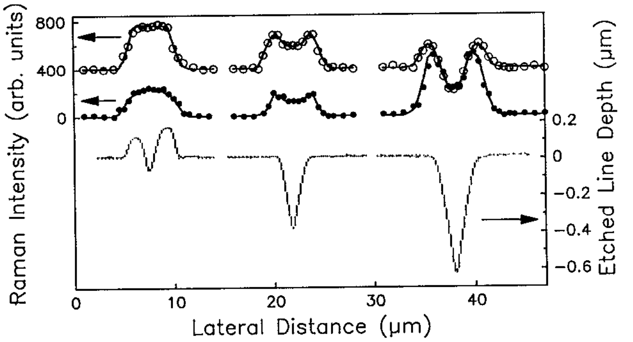

FIG. 16. Raman microprobe and profilometry traces across laser-melted lines representing the three different processing regimes. The left, middle, and right columns correspond to regimes I, II and III, respectively (1.6 W; I-mixture A, 180 μm/s; II-mixture B, 60 μm/s; III-mixture B, 5 μm/s). The top (open circles) and middle (solid circles) traces are the $z(x,y)\bar{z}$ and $z(x,x)\bar{z}$ Raman traces (~0.005 W), respectively, taken after processing, while the bottom traces are the profilometry profiles.

Real-time monitoring of melting and melt-induced etching was reexamined with $z(x,x)\bar{z}$ and $z(x,y)\bar{z}$ analysis, except with the laser scanning along the *y* direction (perpendicular to the *x* laser polarization) instead of along the *x* direction. Very similar spectra were obtained with the same peak frequencies, except that now the Raman peak during etching is larger than during melting for $z(x,x)\bar{z}$ analysis, while it is smaller for $z(x,y)\bar{z}$. Consequently, the difference spectra are negative for $z(x,x)\bar{z}$ and are positive for $z(x,y)\bar{z}$, which is reversed from the results for scanning in the *x* direction. The etch trenches for scanning in the *x* direction are found to be deeper than those obtained by scanning in the *y* direction, as was demonstrated in Ref. 9.

Three etched lines, which are representative of the three etching regimes, were examined after etching both by profilometry and by polarization Raman analysis using a low-power laser beam (0.005 W), as shown in Fig. 16. Profilometry shows that in regime III (mixture B, 1 μm/s), there is a *V*-like deep trench which is ~0.6 μm deep and is ~6 μm wide at the *c*-Si surface and tapers to zero width at the bottom of the trench. In regime II (mixture B, 60 μm/s), the trench shape is almost the same except that the depth is ~0.4 μm and the width at surface is ~3 μm. The trench shape obtained by profilometry in regime I (mixture A, 180 μm/s) is much different than those for regimes II and III. It is similar to the profile of a melted line with no Cl_2 present and has a trench at the center which is ~0.1 μm deep and ~ 1 μm wide. There are raised ridges on either side, which are not present after melt-induced etching, that are ~0.2 μm high and ~2.7 μm wide.

The Raman scans across these three etched lines are quite different for the different regimes. In this post-melt Raman analysis, only $z(x,y)\bar{z}$ signals are seen outside the melt region, while within the resolidified region both

$z(x,y)\bar{z}$ and $z(x,x)\bar{z}$ signals are seen that are larger than the $z(x,y)\bar{z}$ peak in *c*-Si. Note the characteristic dip at the center for both x and y polarizations in regimes II and III, which is absent in regime I and in melting (only) scans. The lateral linewidth determined by Raman profiling is greater than that determined by profilometry for regimes II and III, but they are close for regime I. The Raman shifts and linewidths within the trench are within 0.5 cm^{-1} of the respective values for *c*-Si.

E. Laser etching of Ge with a scanning laser

Germanium has also been shown to undergo etching by both laser-assisted thermal and photochemical processes.[34] The etching of Ge by localized laser heating in the presence of chlorine was examined briefly. In contrast to silicon, laser-heated Ge was found to etch rapidly even when not partially molten. Raman analysis was not used to probe laser etching of Ge.

IV. DISCUSSION

A. Laser heating with a static laser—no melting

With no melting, the temperature peaks at the center of the heating laser, which has a ~ 1 μm spot size, and decreases with a characteristic distance of $\sim$1–2 μm.[35] Since this laser also probes the temperature profile, the Raman profile represents an average of a range in temperatures. As P approaches P_m, the temperature at the center approaches the melting temperature. Because of spatial averaging, the Raman shift approaches $\sim$510 cm^{-1} in Si (Fig. 1) and not the 482 cm^{-1} shift expected for solid Si that is uniformly heated to the melting temperature. Using the Raman profile simulation from Ref. 31, the predicted Raman shift for $P \lesssim P_m$ is 511.2 cm^{-1}. Similarly, the shift in laser-heated Ge approaches 292 cm^{-1} (Fig. 3) and not the 281 cm^{-1} expected for Ge that is uniformly heated to melting.[28,31] Because the fractional decrease in thermal conductivity from 295 K to the melting point is larger in Si than in Ge, the temperature increase is slightly more localized in Si than in Ge.[36] This explains why the *c*-Si Raman spectra are asymmetric, while the *c*-Ge spectra are nearly symmetric, and has been confirmed by Raman profile simulations similar to those performed in Ref. 31. As alluded to in Sec. III A, this asymmetric profile in silicon was used to model the high-energy peaks in $z(x,y)\bar{z}$ Raman spectra of partially molten Si.

Since the thermal conductivities (K) of silicon, sapphire, and quartz are related by $K_{\text{Si}} > K_{\text{sapphire}} > K_{\text{quartz}}$, the temperature profiles are increasingly more uniform for laser-heated *c*-Si, silicon films on sapphire, and silicon films on quartz.[31] Consequently, the Raman shifts for laser powers P_m are expected to be successively smaller (and nearer 482 cm^{-1}) for these three cases,[31] as is observed here.

Because of temperature averaging in these experiments, the measurement of a Raman shift during local laser melting of *c*-Si that is $\ll$510 cm^{-1} strongly suggests that a significant fraction of the probed silicon is solid material pegged at the melting temperature.

B. Laser melting with a static laser—in vacuum

When melting occurs ($P \gtrsim P_m$), a central region with coexisting solid and liquid phases is expected to form initially, in which the temperature is nearly uniform and is very nearly equal to the melting temperature (T_m). This area is surrounded by a hot solid zone that retains the symmetry of the crystal. This central region is much smaller ($\sim$1–20 μm diameter) than the $\sim$40–500 μm diameter regions that were made partially molten in silicon films in previous studies.[10–13] Using the estimates by Hawkins and Biegelsen for silicon,[12] very narrow solid lamellae with widths $\sim$0.3 μm are expected to float within this central region and the local temperature variation between solid and liquid regions is expected to be $\sim$2 K. Free pieces of solid silicon are expected to float to the surface because at the melting point the density of solid Si is less than that of liquid Si.

For $P \gg P_m$, the central region can be totally molten and the temperature can greatly exceed the melting temperature. The decrease of Raman intensity in partially molten Si with increasing P suggests that less of the surface is covered with solid Si at higher laser powers. For $P > 0.7$ W ($t = 0$–5 s), no Raman peaks are seen for Ge, suggesting that it is totally molten.

The single $z(x,x)\bar{z}$ peak and the low-energy $z(x,y)\bar{z}$ peak are due to solid silicon and germanium no longer in (001) orientation ($t = 0$–0.5 s). For early t, these peaks are probably due to randomly oriented solid regions at the melting temperature floating in the molten region, and not due to hot resolidified polycrystalline (or otherwise reoriented) regions. The outer solid zone is probed by the wings of the laser, leading to the high-energy peak in $z(x,y)\bar{z}$ analysis (0–0.5 s) that is absent in $z(x,x)\bar{z}$ analysis of such crystalline materials. The peripheral region maintains the symmetry of *c*-Si and represents a range of temperature; the highest temperature is at the periphery of the central zone (the melting temperature) and it then decreases outwards.

The Raman probe depth, which is $\sim 1/(2\times$ absorption coefficient), is $\sim$160 Å for solid Si (Ref. 37) and $\sim$40 Å for molten Si,[38] both at the melting temperature for 5145 Å. If the partially molten region is thin enough, it is possible that *c*-Si under the partially molten zone may also contribute to the high-energy peak in the $z(x,y)\bar{z}$ spectrum. This would also apply to the Raman spectrum during laser melting of *c*-Ge.

As laser heating continues in *c*-Si, this high-energy $z(x,y)\bar{z}$ peak moves to lower frequency and decreases in magnitude, which suggests that the partially molten pool is expanding radially. After $\sim$5 s, this expansion has progressed to the point where the laser probes only material in the partially molten pool, and possibly solid silicon beneath it, and there is only a single peak seen for $z(x,y)\bar{z}$. For $t \gtrsim 5$ s, both the $z(x,x)\bar{z}$ and $z(x,y)\bar{z}$ spectra consist of a single peak whose shift increases quickly until t_1 and then increases more slowly to 502 cm^{-1} until t_2. This indicates that the average temperature in the probed region is continuing to decrease. Also, there is rapid molten flow (as determined by profilometry) and a swirling reflection pattern until $\sim t_1$. Then there is still slow flow of molten silicon until $\sim t_2$, while the reflection pattern continues to fluctuate mildly. At t_2, the Raman peak finally stops at $\sim 502\ \text{cm}^{-1}$, which is much less than the $\sim 510\ \text{cm}^{-1}$ peak expected for a silicon substrate that is heated by the laser to T_m. The reflection pattern continues to fluctuate for $t > t_2$, suggesting that the laser-heated spots are still partially molten for $t > t_2$, but that the flow has reached a steady-state profile where the capillary effect counters the surface tension gradient. Note that in these experiments Raman scattering probes a region whose depth and liquid/solid ratio may vary with time.

The depth of these structures is $\sim 1\ \mu\text{m}$. Given the small degree of defocusing at this depth, to a spot size $\sim 1.1\times$ that at the focus (as determined by beam profiling), one would expect melting to continue for the $P \gg P_m$ experiments depicted in Figs. 5–7. Note that the temperature rise $\propto$ 1/laser spot size, assuming temperature-independent parameters and no phase transitions.[35] The swirling reflection pattern would be expected to end when a steady-state surface profile is reached during irradiation. The small fluctuations seen in reflection for $t > t_1$ are consistent with continued melting. This fluctuating reflection pattern is still observed as the laser power is reduced until the Raman shift has increased to $\sim 510\ \text{cm}^{-1}$. Both the Raman and reflection observations indicate that melting has then stopped.

When reexamined by Raman spectroscopy using very low laser power after laser melting, both $z(x,x)\bar{z}$ and $z(x,y)\bar{z}$ have a single Raman peak near $520\ \text{cm}^{-1}$, which suggests that the remaining top layer has solidified from the melt and has become polycrystalline (or misoriented from the original crystal direction). Refraction effects that may contribute to a $z(x,x)\bar{z}$ signal, as described in the Introduction, do not seem to be very important in the polarization analysis.

For *c*-Ge, the shift in the $z(x,x)\bar{z}$ Raman peak is independent of laser power and time (for $t = 0$–10 s). For *c*-Si, this peak is at $502\ \text{cm}^{-1}$ just above the melting threshold (0–0.5 s) and then decreases with increasing P, remaining at the constant value $\sim 482\ \text{cm}^{-1}$ for a wide range of laser powers (0.9–1.8 W). For each laser power, the Raman shift then increases with time. Since any compressive stresses on silicon would increase the Raman shift, as would the probing of cooler material, the measurement of a minimum Raman shift at $482\ \text{cm}^{-1}$ and the observed polarization properties suggest that solid silicon is freely floating in a molten bath during the early stages of laser heating with $P = 0.9$–1.8 W. Because the Raman probe depth is so small for molten silicon, solid silicon lying below any melt may not be probed when the solid silicon at the surface is freely floating in a melt. The increase in frequency shift at later times may indicate that these solid regions are no longer freely floating and pinned at the melting point, and possibly also that the melt has become very shallow with the flow of molten silicon away from the center. For $P = 0.4$–0.9 W, the melt may already be too shallow early during melting (even before molten flow) for there to be freely floating silicon pinned at T_m.

Compressive stresses that occur during laser heating of solid silicon (up to T_m) cannot change the Raman shift by more than $\sim +1\ \text{cm}^{-1}$.[39] Stresses applied to solid material in the liquid bath are certainly much smaller and will perturb the Raman spectrum only slightly. Therefore, the Raman shifts and linewidths at the melting temperature cited here and in Ref. 28 represent relatively stress-free conditions.

When solid silicon at the surface does not float freely, Raman probing will examine this near-surface silicon, which may be at or near the melting temperature, as well as the solid and possibly recrystallized silicon beneath it, which will be cooler. This is probably the principal reason for the larger $z(x,x)\bar{z}$ Raman shifts at lower powers initially (0.4–0.8 W) and at all powers at later times. In all cases, the laser is continuously being defocused on the receding surface during the flow of molten silicon, and the laser probes an increasingly cooler temperature profile. Stress-induced perturbations in solid silicon ($\sim +1\ \text{cm}^{-1}$), though of the correct sign, are too small to be responsible for the large positive deviations ($\sim +10\ \text{cm}^{-1}$) from a $482\ \text{cm}^{-1}$ shift in these regimes of laser melting.

The vapor pressures of Si and Ge at their melting temperatures are 3.8×10^{-4} and 8.0×10^{-7} Torr, respectively.[40] When the ambient pressure is less than this vapor pressure, the surface will evaporate at a rate of $1.2\times10^{-2}\ \mu\text{m/s}$ for Si and $2.1\times10^{-5}\ \mu\text{m/s}$ for Ge. Under the "vacuum" conditions here, this may be significant only for Si. Profilometry shows that after the silicon was melted using high laser power (1.6 W) in vacuum for a long time (~ 200 s), a 1.5-μm-deep pit is seen at the center which is 10 μm wide at both the top and bottom surfaces. Such a deep pit is not seen with argon added. Since silicon evaporates at a rate of $\sim 0.7\ \mu\text{m/min}$ at T_m, this deep hole may be due to evaporation in addition to molten flow. No signs of significant evaporation can be seen during laser melting of *c*-Ge.

Thermal steady state in *c*-Si and *c*-Ge is reached during the first 0.1–1 μs of laser heating when $P < P_m$.[41] For $P > P_m$, the characteristic time for the propagation of the melt front in silicon is 10–100 μs for $\sim 1\ \mu\text{m}$ dimensions,[16] assuming no flow of the molten silicon. These characteristic times are much shorter than the typical measurement times in the static heating experiments and the laser dwell times in the scanning experiments. Flow of molten silicon occurs with a characteristic timescale of ~ 10 s in the static heating experiments. In the scanning laser runs, molten flow is observed even with a ~ 10 ms dwell time. Potential evaporation of Si in vacuum would take ~ 100 s to form a measurable depth ($\sim 1\ \mu\text{m}$).

The Raman spectra taken during laser melting of silicon thin films can be interpreted in the same way at the *c*-Si Raman spectra. For epi Si on sapphire, single peaks are observed for partially molten Si for $z(x,x)\bar{z}$ analysis, while double peaks are seen for $z(x,y)\bar{z}$. These two peaks are well resolved because the peak from the silicon pieces in the melt (at $482\ \text{cm}^{-1}$) is well separated from the high-energy peak due to the nonuniformly heated, nonmelted silicon on sapphire.[31] At high laser power ($P > 0.7$ W), evidence of silicon flow is seen even for $t = 0$–0.5 s with the loss of the low-energy Si peak (Fig. 2) and the appearance of the Raman peak of sapphire. As expected, the Raman spectrum of laser-melted poly Si on sapphire has two peaks for both $z(x,x)\bar{z}$ and $z(x,y)\bar{z}$ analyses.

Because of the low thermal conductivity of quartz, the temperature profile during laser heating of silicon films on this substrate is broad ($P < P_m$)[31] and the Raman peak approaches ~ 499 cm^{-1} as P approaches P_m. This would be similar to the high-energy peak expected for $z(x,y)\bar{z}$ Raman analysis during laser melting of silicon films on quartz. However, because this peak is so low in energy and so broad it overlaps the low-energy peak near 482 cm^{-1} to form a single peak. The increase in the Raman shift to 512 cm^{-1} during melting of silicon films on quartz with $P > 0.3$ W suggests that the silicon has flowed away from the laser focus during the first 0.5 s of laser melting.

C. Laser melting with a static laser—in a gas

Gas above the laser-heated surface can affect the temperature profile, surface tension, molten flow, and the evaporation rate. The previous discussion has shown that the evaporation of Si and Ge is never significant in these experiments in the presence of a gas.

The solution of the heat flow equation during steady-state laser heating of a semi-infinite solid in vacuum is easily modified to include thermal conduction to a gas by treating the gas as a transparent semi-infinite region.[42] At the center of the laser spot on the surface, which is the hottest place in the heated material, the temperature rise is

$$\Delta T_{\text{with gas}} = \frac{K_{\text{Si}}}{K_{\text{Si}} + K_{\text{gas}}} \Delta T_{\text{vacuum}}, \qquad (1)$$

where K is the thermal conductivity of the medium, which is assumed to be independent of T, and ΔT_{vacuum} is the temperature rise in vacuum. Since K_{Si} actually varies with T, the maximum effect of the gas may be estimated by setting K_{Si} equal to the lowest thermal conductivity of solid silicon in the temperature range of interest, i.e., that at the melting point.[43] This expression predicts that adding 1 atm of He or Ar decreases the temperature rise for a given laser power by no more than 0.8% or 0.1%, respectively, or equivalently, that the presence of the gas increases the power needed to achieve melting by these same percentages. The observed differences, 12%–15%, are much larger, suggesting that other effects must be important. Foremost is probably convective flow, which is ignored in the thermal diffusion calculation and which would cool the surface very effectively.

Experimental uncertainties in published data for surface tensions in vacuum and in the presence of a gas are too large to determine the effect of a gas on surface tension γ. An upper limit of this effect may be estimated by McLeod's empirical equation for the surface tension of a surface in contact with a gas of the same molecules, $\gamma \sim (\rho_l - \rho_v)^4$, where ρ_l and ρ_v are the liquid and vapor densities, respectively.[44] Introduction of 200 Torr of Si to a Si surface at 1690 K would be expected to decrease the surface tension by 0.008%; 200 Torr of added Ar should have an even smaller effect. For comparison, near the melting point the same fractional decrease in silicon surface tension occurs for a temperature increase of only 0.4 K.[44] This would suggest that the introduction of any gas should have very little effect on the dynamics of molten flow in these experiments.

In contrast to these expectations, the presence of argon definitely affects laser melting, as is seen by the real-time Raman scattering and the profilometry results. Notably, higher Raman frequency shifts are measured when argon is added to the vacuum for both Si (Fig. 9) and Ge, and molten flow is affected, particularly in Ge (as determined by profilometry). Perhaps, the temperature rise during laser heating is lower in many regions with added argon vis-a-vis vacuum because of convective flow, and this can slow down the flow of the molten semiconductor from the central region.

The increasing line shift of the $z(x,x)\bar{z}$ Raman peak during static laser melting in vacuum or argon in Figs. 5 and 9 must indicate gradual cooling in the central region, which is caused by the flow (and possible evaporation) of silicon or germanium from the center and by laser defocusing. This behavior is clearly different in the presence of argon and in vacuum. The molten layer, which may be ~ 1 μm thick initially, is getting thinner with time and the underlying silicon will be probed more with time. The thickness of this layer may be affected by the buffer gas.

D. Laser melting and etching with a scanning laser

The threshold for melting P_m increases with scan speed and with argon pressure. The latter effect can be attributed to enhanced convective cooling of the surface. The origin of the dependence on scan speed is less clear. Since the laser dwell time at any spot during the scan is always much shorter than the thermal diffusion time in silicon for these experiments, the increased P_m with scan speed does not appear to be attributable to changes in thermal conduction. It is possible that near threshold the time required for melt-initiated surface changes (that affect the reflection pattern) may be longer than the laser dwell time. Consequently, the quoted values for P_m at faster scan speeds may be slightly too high.

The Raman spectrum during melting by a scanning laser always has a single peak. This differs from the static beam experiments for which there are two peaks for $z(x,y)\bar{z}$ polarization. The single peak nature suggests that there is no steady-state bimodal temperature distribution during scanned melting; whereas, during static heating there are large surface areas covered by solid pieces of Si pegged to the melting temperature T_m and also significant areas of Si at $T < T_m$ being probed.

The $z(x,x)\bar{z}$ peaks are generally much smaller the $z(x,y)\bar{z}$ peaks during scanned melting, while the individual peaks are comparable to each other during static laser melting. For slow scan speeds, ~ 20 μm/s, the integrated $z(x,x)\bar{z}$ Raman intensity is roughly half that of the $z(x,y)\bar{z}$ spectrum; this is the same ratio as during static melting

(0–0.5 s). However, with increasing scan speed the ratio of the integrated $z(x,x)\bar{z}$ intensity to that of $z(x,y)\bar{z}$ decreases by a factor of ~ 3. Still, the $z(x,x)\bar{z}$ Raman peaks are much larger than any signal expected from the 1% y-polarization leakage into the x-polarization channel and they also look very different than the $z(x,y)\bar{z}$ peaks; for example the $z(x,x)\bar{z}$ signals always have relatively smaller shifts. Since the $z(x,x)\bar{z}$ peaks are relatively smaller, parts of the region being probed maintain the orientation of the c-Si lattice. It may also mean that these solid pieces may not rotate much while the laser dwells at any point in the scan for fast scanning speeds (~ 10 ms, 200 μm/s), though they may rotate during the ~ 0.1 s dwell times for slower scan speeds and the 0.5 s measurement time of the static experiments.

The $z(x,x)\bar{z}$ and $z(x,y)\bar{z}$ Raman peaks during scanned laser-induced melting and etching lie between the Raman shift of c-Si at the melting temperature (482 cm^{-1}) and the $z(x,y)\bar{z}$ Raman shift obtained for $P \lesssim P_m$ (~ 510 cm^{-1}). As stated earlier, this is a signature of Raman probing of laser melting in c-Si. In addition to having smaller heights, the $z(x,x)\bar{z}$ peaks have smaller shifts than the $z(x,y)\bar{z}$ peaks at each scan speed (Fig. 11). This indicates that the reoriented silicon probed by $z(x,x)\bar{z}$ analysis is relatively hotter. For both polarizations, the general trend of increasing Raman shift with scan speed, which is most notable at slower speeds, suggests that the probed distributions are slightly cooler on the average at fast scan speeds.

Raman shifts for $z(x,x)\bar{z}$ analysis during etching are larger than during pure melting, though they still lie between 482 and 510 cm^{-1} (Fig. 11). This is true whether the laser scans in either the x or y direction and suggests that the reoriented solid silicon being probed during etching is on the average cooler than during melting. This is reasonable since the laser is more defocused on the surface during etching and therefore the probed region will be cooler.

The relative size of the Raman signals during melting and etching is determined by the laser and Raman photon transmission probabilities, which depend on the details of the trench geometry and on photon polarization. Careful comparison of the Raman spectra taken during melting and etching, including the detailed analysis of the difference spectra, requires proper calibration of the relative amplitudes of these spectra. Because the relative calibration factor is on the order of unity, the difference spectrum still provides some qualitative insight even without more careful calibration. Using Fig. 14, the $z(x,x)\bar{z}$ difference spectrum peaks near 482 cm^{-1} at slow scan speeds where the etch trenches are deep. At the scan rate increases and the etched trenches become shallower, the difference spectrum lineshift increases and its magnitude decreases (Figs. 13–15). These trends are independent of photon polarization and are relatively insensitive to calibration. Similar trends are seen for $z(x,y)\bar{z}$ and for both polarizations when the laser scans in the y direction. (Note, however, that without amplitude calibration the range over which the difference peak lineshift varies with scan speed is different for each polarization and scan direction arrangement.)

These difference Raman spectra get smaller as the scan rate increases into regime I. Moreover, the dependence of the difference spectrum peak height on scan speed in Fig. 15 tracks that of the etch depth in Fig. 13. This is understood by the increased defocusing of the laser and consequently decreased laser heating with increasing etch depth. The decrease in difference spectrum peak height and its change in sign at very slow scan speeds (Fig. 15, mixture B) is probably due to changing photon transmission factors for these very deep grooves. Though features of the difference spectrum do correlate with the etch depth and can provide a qualitative real-time measurement of etch depth, *ab initio* determination of the etch depth from the Raman spectrum requires more detailed modeling.

Treyz *et al.*[9] showed that changing the angle between the polarization of the incident laser and the scan direction in melt-assisted etching of c-Si by Cl_2 can change the etch rate and trench geometry. This is due to the different transmission factors of the laser into the silicon for each polarization and depends on the details of the etch trench geometry. One consequence of this effect is that etched trenches are deeper when the scan direction and laser polarization are parallel than when they are perpendicular. The parallel polarization is π polarization with respect to the leading surface of the reaction front and is transmitted more than the perpendicular σ-like light, and therefore heats the silicon more. Similarly, the Raman scattering signal depends on the product of this factor for laser transmission into Si and the transmission factor for Raman scattered photons leaving Si. These factors may be different during pure melting and melting-induced etching because they are determined by the etch depth and profile and by the position of the scanning laser relative to the etch front.

The Raman peak intensity is larger during melting than during etching when the Raman polarization is parallel to the scan direction [x scan direction, $z(x,x)\bar{z}$; y scan, $z(x,y)\bar{z}$], while the peak during etching is relatively larger when the Raman polarization is perpendicular to the scan direction [x scan, $z(x,y)\bar{z}$; y scan, $z(x,x)\bar{z}$]. As the angle of incidence increases at a planar interface (up to Brewsters angle and corresponding to deeper etched grooves) the transmission of σ-polarized light decreases, while that of π-polarized light increases. This would suggest that the photons delivered for and collected from Raman scattering are σ-like for the parallel configuration and π-like for the perpendicular configuration. If so, this implies that the observed Raman scattering is predominantly from probing the side walls of the etch front and is relatively less from the leading surface of the reaction front.

The data in Figs. 13, 15, and 16 show that the *ex situ* profilometry traces, real-time Raman analysis, and post processing Raman profiles have distinctive features in each of the three regimes described in Sec. III D. Using this information, the relative etch depth during etching can be obtained by examining the $z(x,x)\bar{z}$ Raman spectrum in real time.

Raised outer ridges are always observed after static or scanned laser melting of c-Si in vacuum or with an inert gas present. These raised features are never seen in the etching regimes II and III. This suggests that molten silicon is etched before it can flow in these experimental regimes.

V. CONCLUDING REMARKS

By examining Raman scattering from optical phonons in solid silicon, information about the temperature distribution and the profile of the surface during laser melting and melting-assisted etching of this semiconductor can be obtained. This method is applicable to germanium and other semiconductors as well. Though determining the exact details of etching and melting by using only Raman data is difficult, real-time Raman microprobe analysis is still one of the few useful probes of small area processing.

When coupled with the other diagnostic methods used here, Raman scattering is valuable in characterizing and explaining different aspects of these processes. For instance, it has been shown that when a single cw laser (fixed or scanning) is used to heat and Raman probe silicon, local melting is indicated when the Raman peak is between 482 cm^{-1}, which is the Raman shift for silicon uniformly heated to the melting point (1690 K), and $\sim$510 cm^{-1}, which is the Raman shift for *c*-Si heated just to the melting point and probed by the same beam. Local laser melting has been shown to evolve in time and to depend on local gas conditions much more than would be expected from simple thermal conduction considerations. Further, the etch depth during local laser etching by a scanning laser has been shown to be related to the difference of the real-time Raman spectra during melting (only) and etching. For best analysis, these Raman measurements must be linked to detailed process modeling of heat flow and mass transfer.

In conclusion, it is also noted that the two-peak Raman spectrum shown in Fig. 4 and the asymmetric Raman profile seen during scanned laser melting resemble the very broad and asymmetric Raman spectra observed in an earlier study of Raman probing during laser direct writing of Si.[45] The interpretation offered here for such a Raman spectrum implies that partially molten silicon was being deposited during laser writing.

ACKNOWLEDGMENTS

The authors would like to acknowledge support by the Office of Naval Research and IBM, and to thank J. A. Tuchman and P. Leong for assistance in data analysis. M. Thompson, R. Osgood, D. Biegelsen, G. Olson, R. Lemons, and H. van Driel are thanked for discussions concerning laser heating and melting of silicon.

[1] J. B. Lasky, J. Appl. Phys. **53**, 9038 (1982).

[2] R. F. Wood and G. E. Giles, Phys. Rev. B **23**, 2923 (1981).

[3] P. S. Peercy, M. O. Thompson, and J. Y. Tsao, Appl. Phys. Lett. **47**, 244 (1985).

[4] M. O. Thompson, P. S. Peercy, J. Y. Tsao, and M. J. Aziz, Appl. Phys. Lett. **49**, 558 (1986).

[5] For example, see H. E. Cline, J. Appl. Phys. **55**, 2910 (1984); T. I. Kamins, K. F. Lee, and J. F. Gibbons, Appl. Phys. Lett. **36**, 550 (1980).

[6] R. F. Wood and G. A. Geist, Phys. Rev. B **34**, 2606 (1986).

[7] F. Foulon, E. Fogarassy, A. Slaoui, C. Fuchs, S. Unamuno, and P. Siffert, Appl. Phys. A **45**, 361 (1988).

[8] G. J. Galvin, M. O. Thompson, J. W. Mayer, R. B. Hammond, N. Paulter, and P. S. Peercy, Phys. Rev. Lett. **48**, 33 (1982).

[9] G. V. Treyz, R. Beach, and R. M. Osgood, Jr., J. Vac. Sci. Technol. B **6**, 37 (1988); Appl. Phys. Lett. **50**, 475 (1987).

[10] J. S. Preston, H. M. van Driel, and J. E. Sipe, Phys. Rev. Lett. **58**, 69 (1987), and references cited therein.

[11] K. A. Jackson and D. A. Kurtze, J. Cryst. Growth **71**, 385 (1985).

[12] W. G. Hawkins and D. K. Biegelsen, Appl. Phys. Lett. **42**, 358 (1983).

[13] R. A. Lemons and M. A. Bosch, Appl. Phys. Lett. **40**, 703 (1982); M. A. Bosch and R. A. Lemons, Phys. Rev. Lett. **47**, 1151 (1981).

[14] H. E. Cline, J. Appl. Phys. **52**, 443 (1981).

[15] T. R. Anthony and H. E. Cline, J. Appl. Phys. **48**, 3888 (1977).

[16] P. Schvan and R. E. Thomas, J. Appl. Phys. **57**, 4738 (1985).

[17] M. Bertolotti and C. Sibilia, IEEE J. Quantum Electron **17**, 1980 (1981).

[18] J. E. Sipe, J. F. Young, J. S. Preston, and H. M. van Driel, Phys. Rev. B **27**, 1141 (1983).

[19] G. M. Blom, J. Appl. Phys. **54**, 6175 (1983).

[20] R. A. Lemons and M. A. Bosch, Appl. Phys. Lett. **39**, 343 (1981).

[21] G. J. Fisanick, M. E. Gross, J. B. Hopkins, M. D. Fennell, K. J. Schnoes, and A. Katzir, J. Appl. Phys. **57**, 1139 (1985).

[22] C. E. Chang and W. Wilcox, J. Cryst. Growth **28**, 8 (1975).

[23] S. D. Allen, J. Appl. Phys. **52**, 6501 (1981).

[24] C. R. Moylan, T. H. Baum, and C. R. Jones, Appl. Phys. A **40**, 1 (1986).

[25] D. Bauerle, in *Laser Processing and Diagnostics, Chemical Physics*, edited by D. Bauerle (Springer, Berlin, 1984), Vol. 39, p. 166.

[26] D. C. Skouby and K. F. Jensen, J. Appl. Phys. **63**, 198 (1988).

[27] R. Kullmer and D. Bauerle, Appl. Phys. A **43**, 227 (1987); P. Mogyorosi, K. Piglmayer, R. Kullmer, and D. Bauerle, Appl. Phys. A **45**, 293 (1988); R. Kullmer and D. Bauerle, Appl. Phys. A **47**, 377 (1988).

[28] H. Tang and I. P. Herman, Phys. Rev. B **43**, 2299 (1991).

[29] H. W. Lo and A. Compaan, J. Appl. Phys. **51**, 1565 (1980).

[30] J. Raptis, E. Liarokapis, and E. Anastassakis, Appl. Phys. Lett. **44**, 125 (1984).

[31] G. D. Pazionis, H. Tang, and I. P. Herman, IEEE J. Quantum Electron. **25**, 976 (1989).

[32] R. J. Nemanich, D. K. Biegelsen, R. A. Street, and L. E. Fennell, Phys. Rev. B **29**, 6005 (1984).

[33] E. Anastassakis and Y. S. Raptis, J. Appl. Phys. **57**, 920 (1985).

[34] G. P. Davis, C. A. Moore, and R. A. Gottscho, J. Appl. Phys. **56**, 1808 (1984).

[35] M. Lax, J. Appl. Phys. **48**, 3919 (1977); M. Lax, Appl. Phys. Lett. **33**, 786 (1978).

[36] Y. S. Touloukian and R. W. Powell, Ed., *Thermophysical Properties of Matter* (IFI/Plenum, New York, 1970), Vol. 1, pp. 108, 326.

[37] G. E. Jellison, Jr. and F. A. Modine, Appl. Phys. Lett. **41**, 180 (1982).

[38] D. E. Aspnes, *Properties of Silicon* (INSPEC, The Institution of Electrical Engineers, London and New York, 1988), p. 80.

[39] L. P. Welsh, J. A. Tuchman, and I. P. Herman, J. Appl. Phys. **64**, 6274 (1988).

[40] R. E. Honig, RCA Rev. **23**, 567 (1962).

[41] I. Chen and S. Lee, J. Appl. Phys. **54**, 1062 (1983).

[42] H. Tang and I. P. Herman, J. Vac. Sci. Technol. A **8**, 1608 (1990).

[43] R. F. Wood and G. E. Jellison, Jr., *Semiconductors & Semimetals*, edited by R. K. Willardson and A. C. Beer (Academic, New York, 1984), Vol. 23, p. 183.

[44] J. O. Hirschfelder, C. F. Curtiss, and R. B. Bird, *Molecular Theory of Gases and Liquids* (Wiley, New York, 1954), p. 354.

[45] F. Magnotta and I. P. Herman, Appl. Phys. Lett. **48**, 195 (1986); I. P. Herman, F. Magnotta, and D. E. Kotecki, J. Vac. Sci. Technol. A **4**, 659 (1986).